Observation of modulation instability Kerr frequency combs in a fiber Fabry–Pérot resonator

Thomas Bunel, Matteo Conforti, Zoheir Ziani, Julien Lumeau, Antonin Moreau, Arnaud Fernandez, Julien Roul, Auro M Perego, Kenneth K Y Wong, Arnaud Mussot, et al.

▶ **To cite this version:**

Thomas Bunel, Matteo Conforti, Zoheir Ziani, Julien Lumeau, Antonin Moreau, et al.. Observation of modulation instability Kerr frequency combs in a fiber Fabry–Pérot resonator. Optics Letters, 2023, 48 (2), pp.275-278. 10.1364/OL.479466 . hal-03919688

HAL Id: hal-03919688
https://hal.science/hal-03919688v1

Submitted on 3 Jan 2023

HAL is a multi-disciplinary open access archive for the deposit and dissemination of scientific research documents, whether they are published or not. The documents may come from teaching and research institutions in France or abroad, or from public or private research centers.

L'archive ouverte pluridisciplinaire **HAL**, est destinée au dépôt et à la diffusion de documents scientifiques de niveau recherche, publiés ou non, émanant des établissements d'enseignement et de recherche français ou étrangers, des laboratoires publics ou privés.

Observation of modulation instability Kerr frequency combs in a fiber Fabry-Pérot resonator

THOMAS BUNEL[1,*], MATTEO CONFORTI[1], ZOHEIR ZIANI[1], JULIEN LUMEAU[2], ANTONIN MOREAU[2], ARNAUD FERNANDEZ[3], OLIVIER LLOPIS[3], JULIEN ROUL[3], AURO M. PEREGO[4], KENNETH K. Y. WONG[5], AND ARNAUD MUSSOT[1]

[1] *University of Lille, CNRS, UMR 8523-PhLAM Physique des Lasers Atomes et Molécules, F-59000, Lille, France*
[2] *Aix Marseille Univ, CNRS, Centrale Marseille, Institut Fresnel, Marseille, France*
[3] *LAAS-CNRS, Université de Toulouse, CNRS, 7 avenue de Colonel Roche, 31031 Toulouse, France*
[4] *Aston Institute of Photonic Technologies, Aston University, Birmingham, B4 7ET, United Kingdom*
[5] *Department of Electrical and Electronic Engineering, The University of Hong Kong, Pokfulam Road, Hong Kong, China*
[*] *Corresponding author: thomas.bunel@univ-lille.fr*

Compiled January 3, 2023

We report the experimental observation of modulation instability induced Kerr frequency comb in an all-fiber Fabry-Perot resonator. We fully characterized in intensity and phase the frequency comb with a commercial 10 MHz resolution heterodyne detection system to reveal more than 125 comb teeth within each of the modulation instability side lobes. Moreover, we were able to reveal the fine temporal structure in phase and intensity of the output Turing patterns. The experimental results are in good agreement with numerical simulations.

http://dx.doi.org/10.1364/ao.XX.XXXXXX

Nonlinear microresonators are extremely appealing devices to generate optical frequency combs (OFCs). Due to their high quality factor, compact design (cavity length of hundred of μm) and low energy consumption, they have attracted significant attention over the last decade [1–4]. They have contributed to enabling many applications like chip-scale dual-comb spectrometers [5], high-speed data transmission [6], or broadband comb generation for self-referencing [7]. Despite these impressive performances, launching and collecting light in these chips is still challenging, requiring advanced fiber coupling devices which is an obstacle for applications. Another way to generate OFCs in resonators consists in using all fiber ring cavities of tens of meters in length, whose effective quality factor can reach several million by including an amplifier within the cavity [8, 9]. Spectra obtained by this technique have comparable widths to those in microresonators, but the line-to-line spacing lies in the MHz range, which is a limit for the many applications cited above (like the dual-comb spectroscopy or the high-speed data transmission). An interesting alternative consists in using all fiber Fabry-Pérot (FFP) resonators of several centimeters in length, which can be connected to photonic devices by using a standard fiber connector with physical contact (FC/PC). Quality factors of 32 million had been reported allowing to generate broadband and stable OFCs with moderate pumping power in this type of resonators [10–13]. Different types of combs can be excited within resonators, which depends on several parameters, including the pump power and the cavity detuning. Modulation instability (MI) combs appear in resonators in the standard generation process of cavity solitons (CSs) under powerfull pumping [2, 14, 15]. Broadband and ultra-stable OFCs exploiting cavity solitons effect had been reported in these devices [10–12]. This reveals a great potential for applications due to their easy connection to fiber devices. However, the generation of CSs combs may be tricky because it requires a bistable operation, high peak power, and specific excitation protocols [2–4, 9, 10]. Due to the fundamental role played by MI in the nonlinear dynamics of resonators, MI had been deeply investigated in fiber ring resonators [16–20]. In FFP resonators, hyperparametric modes enhanced by Brillouin scattering had been reported [13], however, no detailed and clear observation of MI Kerr combs has been reported. In this letter, we focus on MI process in all-fiber Fabry-Pérot resonators mounted with standard FC/PC connectors. We show a pure MI comb finely characterized by the mean of an advanced commercial heterodyne detection system (Brillouin Optical Spectrum Analyser, BOSA) providing the phase and intensity of spectra with a 10 MHz resolution. We reveal the discrete comb structure of these MI combs and the corresponding Turing patterns of only 2.1 ps period, in phase and intensity, in the time domain. The experimental results are in good agreement with the numerical simulations of the governing equations [21–23].

The FFP cavity used for the study is depicted in Figure 1(a). It is made from an optical single-mode fiber (SMF-28) with a fiber length of $L = 6.51$ cm, a group velocity dispersion (GVD) of $\beta_2 = -22.9$ ps^2 km^{-1} at the pump wavelength (1550 nm) and a nonlinear coefficient of $\gamma = 1.2$ W^{-1} km^{-1}. Both fiber ends are mounted in FC/PC connectors and Bragg mirrors are deposited at each extremity with a physical vapor deposition technique, to achieve 99.84% reflectance over 100 nm [24]. Figure 1(b) represents a picture of a connector with its deposited mirror. The

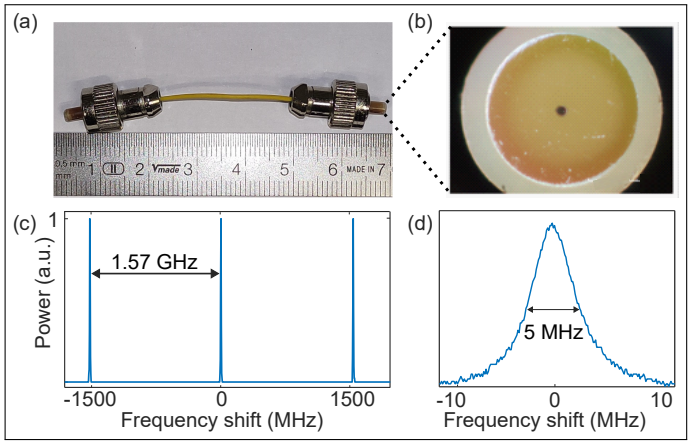

Fig. 1. Description of the studied FFP resonator. (a) Picture of the device. (b) Microscope image of a deposited mirror on the ferule. (c) Transmission function of the resonator in linear regime. (d) Zoom on a cavity resonance.

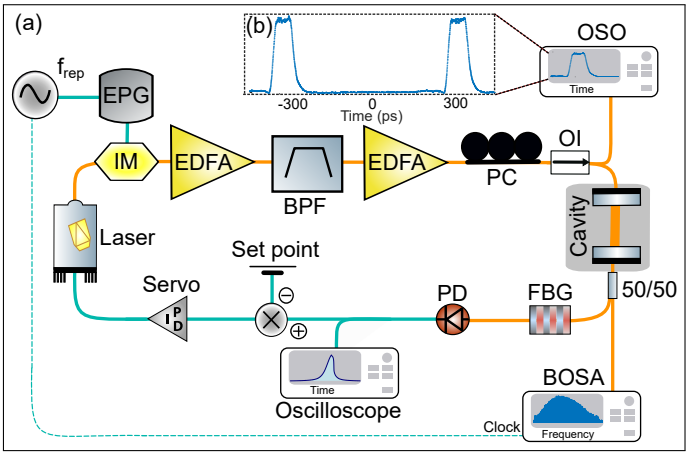

Fig. 2. (a) Experimental setup. EPG: Electrical Pulse Generator; IM: Intensity Modulator; EDFA: Erbium Doped Fiber Amplifier; PC: Polarization Controller; OI: Optical Isolator; FBG: Fiber Bragg Grating; PD: Photo-diode; BOSA: Brillouin Optical Spectrum Analyser; OSO: Optical Sampling Oscilloscope. (b) Pulse train pump measured with the OSO.

linear transfer function is shown in Figure 1(c) and (d). This architecture leads to a resonator with a 5 MHz linewidth resonance, spaced by a free spectral range (FSR) equal to 1.57 GHz, corresponding to a finesse of 314 and a quality factor of 38 million. The parameters of this cavity are comparable to those reported in the literature [10–13]. The great advantage of this resonator is its «plug and play» feature, characteristic of an all-fiber photonic device, which is a very convenient feature compare to ring-microresonator where the coupling can be a real challenge and necessitate a prism fiber taper.

The FFP resonator is implanted in the experimental setup described in Figure 2. A train of 70 ps almost-square pulses [Fig. 2(b)] is generated at 1550 nm by a 0.1 kHz linewidth tunable CW laser (laser BASIK E15 from NKT photonics), and an intensity modulator driven by an electrical pulse generator. The pulses are amplified through two EDFAs, and a filter is used to remove the amplified spontaneous emission in excess at the output of the first amplifier. The pump pulses are finally launched within the cavity through the FC/PC connectors. A frequency synthesizer allows to set the repetition rate very accurately (in the Hz range) in a way that the pulses perfectly overlap in the cavity at each round trip. This pulsed-pump operation allows to reach high intracavity power, necessary to trigger nonlinear effects, with a moderate average power [10], and then, limits the beam fluence sent to the mirrors. A polarization controller is used to send the input signal along one of the polarization axis of the FFP resonator. At the output of the cavity, the signal is split with a 50/50 coupler. One part is used to achieve spectral measurements with a BOSA, a high-resolution (10 MHz) complex optical spectrum analyzer. The second part is monitored with a 5 GHz bandwidth photodiode (Thorlabs DET08CFC/M) and connected to a PID (proportional–integral–derivative) servo to set the laser frequency at a certain detuning. When required, a fiber Bragg grating (FBG), centered at the pump wavelength and of 50 GHz width at FWHM, was used as a notch filter to remove the pump in order to only record the new spectral components generated during the nonlinear process.

In order to analyze the nonlinear dynamics of the system, we scanned the laser across the resonance (from blue to red detuning) as in [2, 10]. Firstly, we record the nonlinear transmission as a function of the frequency detuning, without the FBG [blue line in Fig. 3(a)]. As expected, the nonlinear transfer function is tilted. This phenomenon is accentuated in FP cavity due to the two-way light circulation which induces cross-phase modulation (XPM) [21, 25]. We compared these results with numerics [black dashed line in Fig. 3(a)] (see simulation part below) and found a perfect agreement. In order to focus on the evolution of the new spectral components, we insert the FBG at the cavity output. In this way, we can experimentally identify the detuning range for which new frequency modes are generated. By setting the pump power just above the cavity MI threshold, we see that new spectral components are generated over a very limited frequency range, i.e. cavity detuning [filled yellow curve in Fig. 3(a)]. Hence, MI exists from -2.9 MHz to -5 MHz (compared to the central frequency of the linear resonance). To confirm this, we estimate the frequency range over which the MI process might appear by performing a linear stability analysis as in [22] [filled red plot in Fig. 3(a)]. We find that MI can exist from -2.2 MHz to -3.8 MHz which is very close to the range we measured in experiments. In order to get a deeper insight into the dynamics of this system, we show in Figure 3(b) the evolution of the system for different pump powers. The filled yellow curve in Figure 3(a), corresponding to 4.5 W, is reported in Figure 3(b) for the sake of clarity. Increasing the pump power to 9 W [orange filled curve in Fig. 3(b)] leads to a broadened span of existence of MI without significant modification of the curve shape. This means that MI is the only nonlinear regime involved in the generation of new spectral components. Increasing the pump power to 13 W [blue filled curve in Fig. 3(b)], leads to a significant modification of the curve shape, thus of the dynamics of the system. We observe three different regions [(i), (ii), (iii) in Fig. 3(b)] corresponding to different comb structures according to the classic scan shape where the comb evolves as the function of the detuning [filled blue plot in Fig. 3(b)] [2, 4, 10, 14, 15, 26]. At first (i), the transmission increases with a smooth slope, corresponding to a MI comb formation; (ii) then, chaotic transmission variation appears and produces a chaotic comb; (iii) finally, at the top of the nonlinear resonance, the transmission brutally drops and reach a plateau corresponding to a characteristic step revealing the existence of CSs [4, 26].

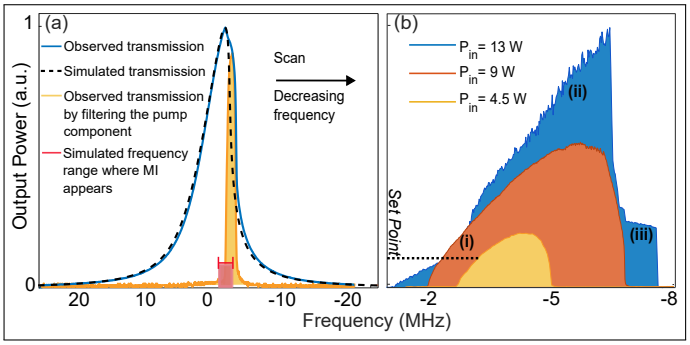

Fig. 3. Transmission functions in nonlinear regime. (a) Measurements with $P_{in} = 4.5$ W. The black dashed line plot is obtained by numerics. The blue solid line plot is obtained by measuring the optical power at the cavity output without any filter. The filled color plots are obtained by filtering the output signal with an FBG to remove the pump component and observe new spectral components evolution. The filled red plot is obtained by calculating the frequency range where MI process appears. (b) New spectral components evolution at different input power.

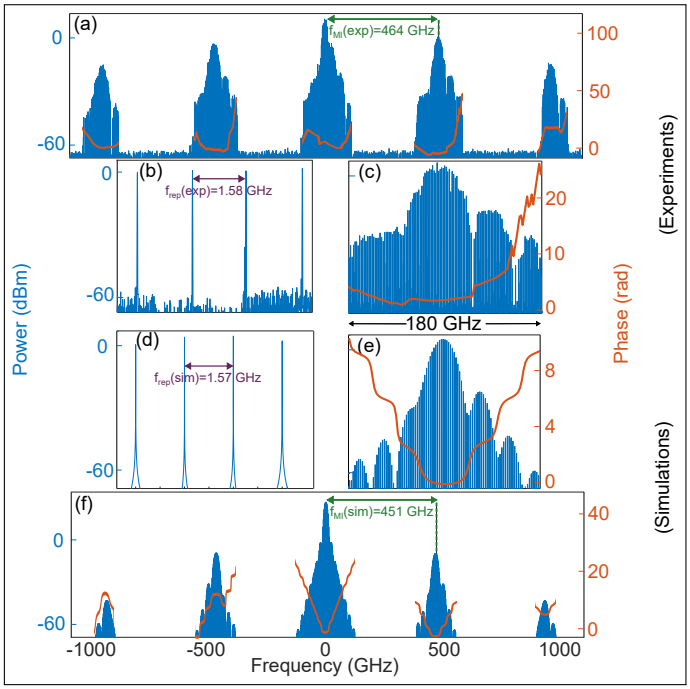

Fig. 4. Observed and simulated spectrum at the resonator output. (a): Full observed MI spectrum. (b): Zoom on the teeth of the observed spectrum. (c): Zoom on an observed MI subcomb. (d): Zoom on the teeth of the simulated spectrum. (e): Zoom on a simulated MI subcomb. (f): Full simulated MI spectrum.

As we aim at investigating modulation instability, we lower the pump power just above the MI threshold (4.5 W). We switch the PID on to set the detuning at -3.5 MHz [Fig. 3(b)]. Thereby, we measured the output complex optical spectra with a BOSA. It is represented in Figure 4(a). We see the two MI bands on each side of the pump shifted by $f_{MI} = 464$ GHz. As the pump power is slightly above the cavity threshold, we also see harmonics at twice this frequency shift which are due to cascaded four-wave-mixing between the MI bands and the pump. An interesting feature lies in the particular shape of the subcombs with a cardinal sinus-like shape [Fig. 4(c)]. We checked numerically that this is due to the square pulse spectrum of the pump which is repeated during the MI process (this feature does not appear during continuous pumping). The high spectral resolution of the BOSA allows for the distinction of each tooth of the frequency subcombs, separated by 1.58 ± 0.062 GHz, which corresponds to the FSR of the cavity [Fig. 4(b)]. Thus, we are able to observe more than 125 teeth in each MI side band with a high signal-to-noise ratio of up to 60 dB [Fig. 4(a) and (b)]. The BOSA also measures the spectral phase of the output signal [orange dots in Fig. 4(a) and (c)]. To obtain these results, we measure the spectral phase on each lobe independently in order to maintain the coherence between each subcomb, and we suppress the linear component caused by a delay in the measurement. One observes that the spectral phase is quite flat even if there are phase jumps between the subcomb's lobes. Using this complex spectrum measurement, we can now calculate the electric field trace in the time domain to reveal the Turing pattern features of the MI process. In Figure 5(a), we see periodic temporal patterns are visible on the top of the pump pulses [blue line in Fig. 5(a)]. The oscillations period is equal to $1/f_{MI} = 2.1$ ps, which corresponds to the inverse of the MI frequency shift [Fig. 4 (a)]. As the BOSA is only able to measure the phase of the spectral envelope, we obtain an unique pulse with Turing patterns at its top. However, we can notice that the complete electric field at the cavity output is composed of a train of this pattern with a frequency equals to f_{rep} (= 1.57 GHz). Concerning, the temporal phase represented in orange lines in Figure 5(a), one observes periodic oscillations with a 2 radians amplitude, in phase opposition with the signal amplitude modulation. Note that in addition to the complex information, the BOSA system allows the observation of short time modulations (2.1 ps), which would not be possible with a system based on a photodiode and an oscilloscope.

In order to validate these experimental results, we performed numerical simulations by solving two coupled counter-propagating nonlinear Schrödinger equations [21, 22]:

$$\frac{\partial F}{\partial z} + \beta_1 \frac{\partial F}{\partial t} + i\frac{\beta_2}{2}\frac{\partial^2 F}{\partial t^2} = i\gamma(|F|^2 + G|B|^2)F \quad \textbf{(1)}$$

$$-\frac{\partial B}{\partial z} + \beta_1 \frac{\partial B}{\partial t} + i\frac{\beta_2}{2}\frac{\partial^2 B}{\partial t^2} = i\gamma(|B|^2 + G|F|^2)B \quad \textbf{(2)}$$

where $F(z,t)$ and $B(z,t)$ are the forward and the backward fields in the cavity, respectively, $\beta_1^{-1} = \frac{c}{n}$ is the group velocity (c and n are speed of light in vacuum and the effective refractive index of the fiber mode), β_2 is the GVD coefficient, γ is the nonlinear parameter and G=2 is the grating-parameter which describes XPM. The governing equations are supplemented with appropriate boundary conditions at the left and right mirrors:

$$F(0,t) = \theta E_{in} + \rho B(0,t) \quad \textbf{(3)}$$

$$B(L,t) = \rho e^{i\phi_0} F(L,t) \quad \textbf{(4)}$$

where, θ and ρ are the transmission and reflection coefficients, respectively; the cavity phase ϕ_0 accounts for the phase acquired during the propagation $\frac{4\pi nL}{\lambda}$ (where λ is the pump wavelength) and any possible contribution from the mirrors. The transmitted field $E_{out}(t)$ can be expressed as:

$$E_{out}(t) = \theta F(L,t) \quad \textbf{(5)}$$

We solved Eqs. (1-4) by means of a finite-difference predictor-corrector scheme [23]. The used parameters are the same as those of the cavity: $\rho = 0.9950$; $\theta = 0.0396$; $\gamma = 1.2 \times 10^{-3}$ W^{-1} m^{-1}; $\beta_2 = -2.29 \times 10^{-26}$ s^2 m^{-1}; $L = 6.51 \times 10^{-2}$ m; n = 1.4582; and $\lambda = 1550 \times 10^{-9}$ m. Figures 4(d),(e),(f) show the numerical results in the spectral domain, to be compared with the experimental ones shown in Figures 4(c),(b),(a), respectively. The output spectrum from numerics is very similar to the experimental one. More specifically, as far as the cardinal sine-like shapes and the phase which is quite flat with phase jumps between the subcomb's lobes [Fig. 4(b) and (d)]. The MI bands are shifted by $f_{MI} = 451$ GHz from the pump which is very close to the experimental measurement (464 GHz). In the time domain [Fig. 5(b)], the period of the modulations is in perfect agreement with the experiments. The modulations exhibit an almost constant intensity in the numerics but vary in experiments. The phase shows a very similar profile to the experiments, except that it is this time in phase with the signal amplitude modulation. These slight discrepancies may be due to small fluctuations in the stabilization system and/or the shape of the input pump pulses not being perfectly flat and/or a slight disagreement regarding the pump power value.

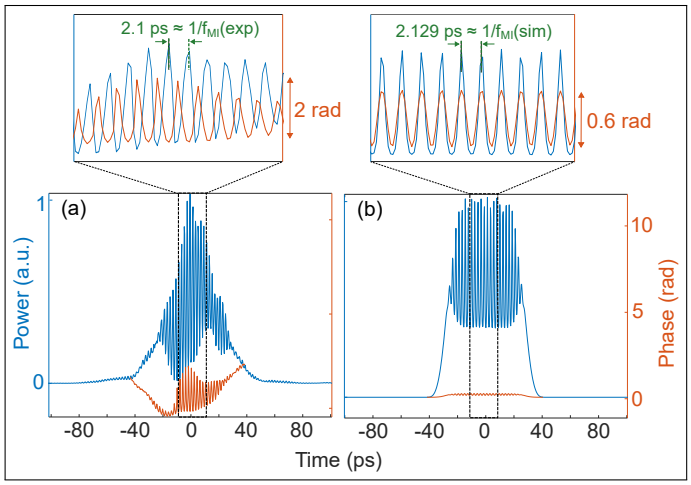

Fig. 5. Full field output pulse. (a) Experiment. (b) Numerics. Blue line: signal amplitude; orange line: temporal phase

In summary, we have studied MI-induced Kerr combs in an all-fiber Fabry-Perot resonator consisting of a standard 6.51-centimeter SMF-28 mounted on FC/PC connectors. Highly reflective mirrors deposited on both connector ferrules lead to a quality factor of 38.5 million, in the same range as for microresonators [2]. We characterized the frequency comb in intensity and phase using a commercial 10 MHz resolution heterodyne detection system (BOSA) to clearly distinguish each tooth of the comb. We then show the fine temporal structure of only 2.1 ps period in phase and intensity of the Turing patterns. These results were confirmed by numerical simulations based on coupled nonlinear Schrödinger equations. This research contributes to a better understanding of the dynamics of the modulation instability process in high Q-factor all-fiber Fabry-Perot resonators.

Funding. The present research was supported by the Agence Nationale de la Recherche (Programme Investissements d'Avenir, I-SITE VERIFICO; and ASTRID ROLLMOPS); Ministry of Higher Education and Research; Hauts de France Council; European Regional Development Fund (Photonics for Society P4S), the CNRS (IRP LAFONI); A.M.P. acknowledges support from The Royal Academy of Engineering throught the Research Fellowship Scheme; and the university of Lille (LAI HOLISTIC)

Acknowledgements. The authors thank B. Kibler for providing the sub-kHz linewidth tunable laser BASIK E15 from NKT photonics, as well as B. Wetzel for fruitful discussions.

Disclosures. The authors declare no conflicts of interest.

Data availability. Data underlying the results presented in this paper are not publicly available at this time but may be obtained from the authors upon reasonable request.

REFERENCES

1. T. Fortier and E. Baumann, Commun. Phys. **2**, 153 (2019).
2. T. J. Kippenberg, A. L. Gaeta, M. Lipson, and M. L. Gorodetsky, Science **361**, eaan8083 (2018).
3. W. Wang, L. Wang, and W. Zhang, Adv. Photonics **2**, 1 (2020).
4. A. Pasquazi, M. Peccianti, L. Razzari, D. J. Moss, S. Coen, M. Erkintalo, Y. K. Chembo, T. Hansson, S. Wabnitz, P. Del'Haye, X. Xue, A. M. Weiner, and R. Morandotti, Phys. Reports **729**, 1 (2018).
5. M.-G. Suh, Q.-F. Yang, K. Y. Yang, X. Yi, and K. J. Vahala, Science **354**, 600 (2016).
6. P. Marin-Palomo, J. N. Kemal, M. Karpov, A. Kordts, J. Pfeifle, M. H. P. Pfeiffer, P. Trocha, S. Wolf, V. Brasch, M. H. Anderson, R. Rosenberger, K. Vijayan, W. Freude, T. J. Kippenberg, and C. Koos, Nature **546**, 274 (2017).
7. J. D. Jost, T. Herr, C. Lecaplain, V. Brasch, M. H. P. Pfeiffer, and T. J. Kippenberg, Optica **2**, 706 (2015).
8. F. Leo, S. Coen, P. Kockaert, S.-P. Gorza, P. Emplit, and M. Haelterman, Nat. Photonics **4**, 471 (2010).
9. N. Englebert, C. Mas Arabí, P. Parra-Rivas, S.-P. Gorza, and F. Leo, Nat. Photonics **15**, 536 (2021).
10. E. Obrzud, S. Lecomte, and T. Herr, Nat. Photonics **11**, 600 (2017).
11. K. Jia, X. Wang, D. Kwon, J. Wang, E. Tsao, H. Liu, X. Ni, J. Guo, M. Yang, X. Jiang, J. Kim, S.-n. Zhu, Z. Xie, and S.-W. Huang, Phys. Rev. Lett. **125**, 143902 (2020).
12. S.-W. Huang, M. Nie, K. Jia, Y. Xie, S. Zhu, and Z. Xie, "Spatiotemporal mode-locking and photonic flywheel in multimode microresonators," preprint, In Review (2022).
13. D. Braje, L. Hollberg, and S. Diddams, Phys. Rev. Lett. **102**, 193902 (2009).
14. S. Coen and M. Erkintalo, Opt. Lett. **38**, 1790 (2013).
15. P. Parra-Rivas, D. Gomila, M. A. Matías, S. Coen, and L. Gelens, Phys. Rev. A **89**, 043813 (2014).
16. S. Coen and M. Haelterman, Opt. Lett. **26**, 39 (2001).
17. S. B. Papp, P. Del'Haye, and S. A. Diddams, Phys. Rev. X **3**, 031003 (2013).
18. M. Conforti, A. Mussot, A. Kudlinski, and S. Trillo, Opt. Lett. **39**, 4200 (2014).
19. M. Conforti, F. Copie, A. Mussot, A. Kudlinski, and S. Trillo, Opt. Lett. **41**, 5027 (2016).
20. F. Copie, M. Conforti, A. Kudlinski, A. Mussot, and S. Trillo, Phys. Rev. Lett. **116**, 143901 (2016).
21. W. Firth, Opt. Commun. **39**, 343 (1981).
22. W. J. Firth, J. B. Geddes, N. J. Karst, and G.-L. Oppo, Phys. Rev. A **103**, 023510 (2021).
23. C. Sun, N. Mangan, M. Dong, H. G. Winful, S. T. Cundiff, and J. N. Kutz, JOSA B **36**, 3263 (2019).
24. J. Zideluns, F. Lemarchand, D. Arhilger, H. Hagedorn, and J. Lumeau, Opt. Express **29**, 33398 (2021).
25. D. C. Cole, A. Gatti, S. B. Papp, F. Prati, and L. Lugiato, Phys. Rev. A **98**, 013831 (2018).
26. T. Herr, V. Brasch, J. D. Jost, C. Y. Wang, N. M. Kondratiev, M. L. Gorodetsky, and T. J. Kippenberg, Nat. Photonics **8**, 145 (2014).

FULL REFERENCES

1. T. Fortier and E. Baumann, "20 years of developments in optical frequency comb technology and applications," Commun. Phys. **2**, 153 (2019).
2. T. J. Kippenberg, A. L. Gaeta, M. Lipson, and M. L. Gorodetsky, "Dissipative Kerr solitons in optical microresonators," Science **361**, eaan8083 (2018).
3. W. Wang, L. Wang, and W. Zhang, "Advances in soliton microcomb generation," Adv. Photonics **2**, 1 (2020).
4. A. Pasquazi, M. Peccianti, L. Razzari, D. J. Moss, S. Coen, M. Erkintalo, Y. K. Chembo, T. Hansson, S. Wabnitz, P. Del'Haye, X. Xue, A. M. Weiner, and R. Morandotti, "Micro-combs: A novel generation of optical sources," Phys. Reports **729**, 1–81 (2018).
5. M.-G. Suh, Q.-F. Yang, K. Y. Yang, X. Yi, and K. J. Vahala, "Microresonator soliton dual-comb spectroscopy," Science **354**, 600–603 (2016).
6. P. Marin-Palomo, J. N. Kemal, M. Karpov, A. Kordts, J. Pfeifle, M. H. P. Pfeiffer, P. Trocha, S. Wolf, V. Brasch, M. H. Anderson, R. Rosenberger, K. Vijayan, W. Freude, T. J. Kippenberg, and C. Koos, "Microresonator-based solitons for massively parallel coherent optical communications," Nature **546**, 274–279 (2017).
7. J. D. Jost, T. Herr, C. Lecaplain, V. Brasch, M. H. P. Pfeiffer, and T. J. Kippenberg, "Counting the cycles of light using a self-referenced optical microresonator," Optica **2**, 706 (2015).
8. F. Leo, S. Coen, P. Kockaert, S.-P. Gorza, P. Emplit, and M. Haelterman, "Temporal cavity solitons in one-dimensional kerr media as bits in an all-optical buffer," Nat. Photonics **4**, 471–476 (2010).
9. N. Englebert, C. Mas Arabí, P. Parra-Rivas, S.-P. Gorza, and F. Leo, "Temporal solitons in a coherently driven active resonator," Nat. Photonics **15**, 536–541 (2021).
10. E. Obrzud, S. Lecomte, and T. Herr, "Temporal solitons in microresonators driven by optical pulses," Nat. Photonics **11**, 600–607 (2017).
11. K. Jia, X. Wang, D. Kwon, J. Wang, E. Tsao, H. Liu, X. Ni, J. Guo, M. Yang, X. Jiang, J. Kim, S.-n. Zhu, Z. Xie, and S.-W. Huang, "Photonic Flywheel in a Monolithic Fiber Resonator," Phys. Rev. Lett. **125**, 143902 (2020).
12. S.-W. Huang, M. Nie, K. Jia, Y. Xie, S. Zhu, and Z. Xie, "Spatiotemporal mode-locking and photonic flywheel in multimode microresonators," preprint, In Review (2022).
13. D. Braje, L. Hollberg, and S. Diddams, "Brillouin-Enhanced Hyperparametric Generation of an Optical Frequency Comb in a Monolithic Highly Nonlinear Fiber Cavity Pumped by a cw Laser," Phys. Rev. Lett. **102**, 193902 (2009).
14. S. Coen and M. Erkintalo, "Universal scaling laws of Kerr frequency combs," Opt. Lett. **38**, 1790 (2013).
15. P. Parra-Rivas, D. Gomila, M. A. Matías, S. Coen, and L. Gelens, "Dynamics of localized and patterned structures in the Lugiato-Lefever equation determine the stability and shape of optical frequency combs," Phys. Rev. A **89**, 043813 (2014).
16. S. Coen and M. Haelterman, "Continuous-wave ultrahigh-repetition-rate pulse-train generation through modulational instability in a passive fiber cavity," Opt. Lett. **26**, 39–41 (2001).
17. S. B. Papp, P. Del'Haye, and S. A. Diddams, "Mechanical control of a microrod-resonator optical frequency comb," Phys. Rev. X **3**, 031003 (2013).
18. M. Conforti, A. Mussot, A. Kudlinski, and S. Trillo, "Modulational instability in dispersion oscillating fiber ring cavities," Opt. Lett. **39**, 4200 (2014).
19. M. Conforti, F. Copie, A. Mussot, A. Kudlinski, and S. Trillo, "Parametric instabilities in modulated fiber ring cavities," Opt. Lett. **41**, 5027 (2016).
20. F. Copie, M. Conforti, A. Kudlinski, A. Mussot, and S. Trillo, "Competing Turing and Faraday Instabilities in Longitudinally Modulated Passive Resonators," Phys. Rev. Lett. **116**, 143901 (2016).
21. W. Firth, "Stability of nonlinear Fabry-Perot resonators," Opt. Commun. **39**, 343–346 (1981).
22. W. J. Firth, J. B. Geddes, N. J. Karst, and G.-L. Oppo, "Analytic instability thresholds in folded kerr resonators of arbitrary finesse," Phys. Rev. A **103**, 023510 (2021).
23. C. Sun, N. Mangan, M. Dong, H. G. Winful, S. T. Cundiff, and J. N. Kutz, "Stable numerical schemes for nonlinear dispersive equations with counter-propagation and gain dynamics," JOSA B **36**, 3263–3274 (2019).
24. J. Zideluns, F. Lemarchand, D. Arhilger, H. Hagedorn, and J. Lumeau, "Automated optical monitoring wavelength selection for thin-film filters," Opt. Express **29**, 33398 (2021).
25. D. C. Cole, A. Gatti, S. B. Papp, F. Prati, and L. Lugiato, "Theory of kerr frequency combs in fabry-perot resonators," Phys. Rev. A **98**, 013831 (2018).
26. T. Herr, V. Brasch, J. D. Jost, C. Y. Wang, N. M. Kondratiev, M. L. Gorodetsky, and T. J. Kippenberg, "Temporal solitons in optical microresonators," Nat. Photonics **8**, 145–152 (2014).